JOM, Vol. 76, No. 6, 2024
https://doi.org/10.1007/s11837-024-06518-1

TECHNICAL ARTICLE

Enhanced Supercapacitive Performance of $FeAl_2O_4$ Nanoparticles with Neodymium (Nd) Doping by Sonication Method

MUKHTIAR HUSSAIN,[1] MEZNAH M. ALANAZI,[2] SHAIMAA A.M. ABDELMOHSEN,[2] MUHAMMAD ABDULLAH,[3] MAHMOOD ALI,[1] SALMA AMAN,[4] ABDULLAH G. AL-SEHEMI,[5,6] A.M.A. HENAISH,[7,8] and HAFIZ MUHAMMAD TAHIR FARID [9,10]

1.—Centre of Excellence in Solid State Physics, University of the Punjab, Lahore 54000, Pakistan. 2.—Department of physics, College of Science, Princess Nourah bint Abdulrahman University, P.O. Box 84428, 11671 Riyadh, Saudi Arabia. 3.—Department of Chemistry, Government College University Lahore, Lahore 54000, Pakistan. 4.—Institute of Physics, Khwaja Fareed University of Engineering and Information Technology, Abu Dhabi Road, Rahim Yar Khan 64200, Pakistan. 5.—Research Center for Advanced Materials Science (RCAMS), King Khalid University, 61413 Abha, Saudi Arabia. 6.—Department of Chemistry, College of Science, King Khalid University, 61413 Abha, Saudi Arabia. 7.—Physics Department, Faculty of Science, Tanta University, Tanta 31527, Egypt. 8.—NANOTECH Center, Ural Federal University, Ekaterinburg, Russia 620002. 9.—Department of Physics, Government Graduate College Taunsa Sharif, Dera Ghazi Khan 32100, Pakistan. 10.—e-mail: tahirfaridbzu@gmail.com

In order to meet the demands of humanity and address the global environmental situation, it is imperative that we explore alternative energy sources and advance energy storage technology. The aim of this study was to investigate the impact of Nd-doping on the structural and electrochemical performance of $FeAl_2O_4$ nanoparticles (NPs). The successful synthesis of Nd-doped $FeAl_2O_4$ NPs) was accomplished through a simple sonication process. An evaluation was conducted on the properties of Nd-doping $FeAl_2O_4$ NPs) to determine their suitability for supercapacitor (SC) applications. Moreover, the specific capacitance (Cs) of Nd-doped $FeAl_2O_4$ NPs) reaches a maximum of 1194.69 F g^{-1} when subjected to a current density of 1.0 A g^{-1} compared to $FeAl_2O_4$ nanoparticles. Furthermore, Nd-doped $FeAl_2O_4$ NPs exhibited excellent cyclic stability and low impedance (R_{ct} = 0.07 Ω), owing to their modified morphology, making a promising material for supercapacitor SC electrodes that offer high capacity, affordability, and environmental friendliness. Our research has validated that the synthesized material can enhance the capacitive properties of transition-metal oxides with spinel structures in new, generated energy storage devices.

INTRODUCTION

There has been a rise in global awareness regarding the importance of energy and the significance of preserving a sustainable environment due to the increasing reliance on fossil fuels.[1–4] There is a growing need for energy systems that are both environmentally friendly and economically viable in the long run. There has been a surge in interest in alternative options, like fuel cells, tidal energy, solar energy, and wind energy.[5–7] However, to guarantee a consistent and dependable power supply from these systems, it is crucial to establish a highly effective storage system. Supercapacitors (SCs) and lithium-ion batteries (LIBs) have been extensively acknowledged as highly promising electrical energy storage technologies. Despite their impressive gravimetric energy density, LIBs still face specific challenges.[8–11] There are certain

(Received February 1, 2024; accepted March 12, 2024; published online April 22, 2024)

factors that affect their performance, including a shorter lifespan, lower energy output, and a slower discharge of stored energy. SCs) have garnered significant attention owing to impressive durability, rapid charge and discharge abilities, exceptional power density, and ability to withstand challenging environments. Furthermore, SCs as electrochemical capacitors act as a bridge between LIBs and regular capacitors.[12–15] LIBs have high specific energy but low specific power, and regular capacitors have high power density but poor energy storage. That is why SCs offer a solution that combines both high power and energy storage capabilities. SCs also have a demonstrated remarkable efficiency in providing power for an extensive range of applications, such as power backup systems, hybrid electronic cars, and portable electronics.[16–20]

In SCs, there are two main groups that may be identified by the way they store charge. They are electrochemical double-layer capacitors that work by capturing electrostatic charges at electrode–electrolyte contact, including graphene and activated carbon materials, and pseudocapacitors (PCs) that employ redox reactions to store charge, such as conducting polymers and transition metal oxide (TMOs).[21–24] However, it was discovered that the energy capacity of SCs is lower compared to LIBs and capacitors. Due to this factor, various electrode materials have been discovered to improve the specific energy of SCs. Recently, there has been much attention paid to the investigation of TMOs with various oxidation states. Because of their low cost, extensive availability, and malleability in terms of both structure and morphology, these oxides are garnering a lot of research interest. Additional characteristics include their high specific capacitance (Cs) and environmental friendliness.[25–27] For this reason, they are being intensively examined as potential SC electrode materials. There has also been a lot of interest in binary TMOs, such as $FeAl_2O_4$,[28] $CuFe_2O_4$,[29] $ZnMn_2O_4$,[30] $NiCo_2O_4$,[31] and $CoFe_2O_4$,[28] as they show promise as electrode materials for PCs. However, $FeAl_2O_4$ is a standout choice among the various options available for TMOs. However, the TMO $FeAl_2O_4$'s wide band gap and poor electric conductivity restrict its potential for electrochemical applications. Effective control of the electrical characteristics is crucial for optimizing the electrochemical properties, which can be accomplished through proper doping procedures. The presence of doped metal ions in TMO composites has led to the creation of multiple electrochemical active sites.[29,30] In addition, the deliberate inclusion of impurities has a notable effect on the number of charge carriers by producing free charge carriers. Recent investigation has shown that the inclusion of the specific impurity of rate-earth ions can significantly improve the electrical, magnetic, and electrochemical characteristics of TMOs.[31,32] This research aims to enhance the electrochemical behavior of these composites for high-performance SCs. This is a result of the strong synergistic behavior exhibited by the metal ions, which ultimately leads to an increase in capacitance values compared to TMOs.[33] Extensive studies have demonstrated that doped TMOs and rare-earth elements possess enhanced electrical and supercapacitor properties. For example, Bhujun et al.,'s studied the effect of Al-doped spinel ferrite, which exhibited high electrical conduction with a Cs of 548 Fg^{-1} at 100 mV s^{-1} with an E_d of 3.84 Wh kg^{-1} and a specific power of 270 Wh kg^{-1}.[34] Monohar et al., synthesized nickel-doped spinel which exhibited a Cs of 119.04 F g^{-1} at 1.1 A g^{-1}.[35] Alahmari et al., prepared Zn-doped $CrVO_4$ which exhibited a Cs of 448 F g^{-1} at 1 mA and an E_d of 54.5 Wh kg^{-1} at a P_d of 1350 W kg^{-1} and a notable efficiency of 99% at the 10,000th cycles.[36]

The synthesis process utilizes Nd as a dopant to modify the morphology and enhance the electrochemical properties. A sonication method was used to prepare binder-free electrodes with Nd-doped $FeAl_2O_4$ active materials grown on conductive Ni foam (NF) substrate. An investigation was conducted to observe the effect of the Nd doping on the performance of electrodes. It is fascinating to observe that the doping of Nd during the sonication preparation alters the morphology of the electrode and incorporates it into the $FeAl_2O_4$ lattice. This leads to the formation of a Nd-doped $FeAl_2O_4$ electrode, which exhibits a significant enhancement in capacitive behavior.

MATERIALS AND METHODS

Reagents

Iron nitrate ($Fe(NO_3)_2{\cdot}9H_2O$, Merk, ≥ 98.99%).), aluminum nitrates ($Al(NO_3)_3{\cdot}9H_2O$, Merk, ≥ 98.997%).), neodymium nitrate $Nd(NO_3)_3{\cdot}9H_2O$, Merk, ≥ 99.9%).), sodium hydroxide (NaOH), deionized water (DI H_2O), and ethanol were utilized as the initial materials. All chemical reagents used in the study were of high quality and used as received.

Preparation of $FeAl_2O_4$ and Nd-Doped $FeAl_2O_4$ Nanoparticles (NPs)

The synthesis of $FeAl_2O_4$ and Nd-doped $FeAl_2O_4$ NPs was carried out using a probe sonicator through sonochemical methods. For the experiment, a 0.1-M solution of $Fe(NO_3)_2{\cdot}9H_2O$ and 0.2 M $Al(NO_3)_3{\cdot}9H_2O$ were synthesized by dissolving in DI H_2O. To achieve a pH level of 11, a 3.0-M NaOH solution was gradually introduced as a precipitation reagent. An ultrasonic probe, controlled by a microprocessor, was used to subject the contents of the beaker to high-intensity ultrasound for a continuous duration of 60 min. As a result of increased molecular collisions, the temperature gradually reached 80°C throughout the process. The resulting precipitate underwent filtration and was subsequently washed with DI H_20. Afterwards, it went through a

drying process for 4 h at 60°C in an electric oven. The final solid product was carefully heated in a furnace for a period of 5 h at a temperature of 450°C.

Figure 1 shows the synthesis of Nd-doped $FeAl_2O_4$ NPs for which the procedure was carried out in the same manner, with the addition of 0.1 M $Nd(NO_3)_3{\cdot}9H_20$ as a dopant.

Material Characterizations

X-ray diffraction (XRD; D/max 2500 PC) diffractograms were attained for structural analysis. Raman spectrometry (JY-HR800) was used to analyze the spectral range of 100–900 cm^{-1} for vibration modes in the crystal. Scanning electron microscopic (SEM; SUPRA-55, JEM-2100) images were recorded with energy-dispersive X-ray analysis (EDX) for elemental composition. Brunauer–Emmett–Teller (BET) and specific surface area analyses were carried out with a TriStar3020 N_2 adsorption/desorption analyzer.

Electrode Assembly and Electrochemical Test

To prepare the electrodes, the material (0.005 g) was sonicated in DI water to create a paste, which was applied onto NF measuring 1.5 × 1.5 cm^2. Subsequently, the electrodes were dried at 60°C to remove any remaining solvents. The electrochemical characteristics were measured utilizing an AUTOLAB PGSTAT-204 workstation in a three-electrode system. The electrodes were composed of platinum wire, Ag/AgCl, and the synthesized material. Numerous electrochemical tests, including cyclic voltammetry (CV) and galvanostatic charge–discharge (more), were measured in 2.0 M KOH electrolyte in an alkaline environment. The CV was conducted at different scan rates (5, 10, 20, and 30 mV s^{-1}) while maintaining a potential of 0.0–0.75 V. However, the Cs was measured using:

$$C_{sp} = \frac{\int_{vs}^{va} I \times dV}{m \times s \times dV} \quad (1)$$

where m is the mass placed (0.005 g) on the NF, potential (ΔV) is the voltage, and s is the sweeping rate, which indicates the speed at which the experiment is being conducted.

The measurement of Cs at current density (1–3 A g^{-1}) by GCD involved using:

$$C_{sp} = \frac{I \times \Delta t}{m \times \Delta V} \quad (2)$$

where I is the applied current, Δt the discharge time, m the loaded mass, and ΔV a change in potential.

Furthermore, Eqs. 3 and 4 can be used to measure the specific energy (E_d) (Wh kg^{-1}) and specific power (P_d) (W kg^{-1}), respectively.

$$E_d = \frac{C_{sp} \times \Delta V^2}{7.2} \quad (3)$$

$$P_d = \frac{E \times 3600}{\Delta t} \quad (4)$$

The impedance characteristics were conducted using electrochemical impedance spectroscopy (EIS) in the range of 0.1–100 kHz.

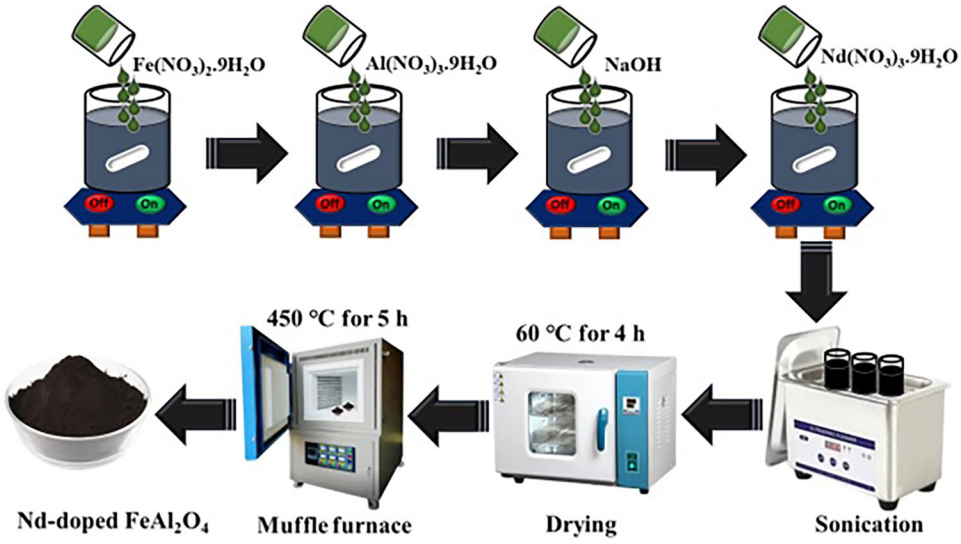

Fig. 1. Synthetic representation of Nd-doped $FeAl_2O_4$ nanoparticles.

RESULTS AND DISCUSSION

Evaluation of Structural Analysis

An investigation of crystal structure of the synthesized material was carried out by XRD, Fig. 2a shows the XRD patterns of $FeAl_2O_4$ and Nd-doped $FeAl_2O_4$ NPs. The diffraction peaks of $FeAl_2O_4$ matched with the standard cubic structure (Fd-3m space group), indicated by JCPDS: 01-086-2320. The peaks observed at specific values of 18.73°, 30.98°, 36.17°, 44.34°, 48.61°, 55.07°, 58.79°, and 64.30° correspond to the lattice planes (111), (2 2 0), (3 1 1), (4 0 0), (331), (4 2 2), (5 1 1), and (4 4 0), respectively. In the XRD pattern of Nd-doped $FeAl_2O_4$ NPs, a slight shifting of peaks was observed which indicates that the Nd^{3+} ion was likely doped into the Fe^{2+} and Al^{3+} sites with strong and distinct peaks, indicating a single-phase and highly crystalline nature. The average crystallite size (D) of the $FeAl_2O_4$ and Nd-doped $FeAl_2O_4$ NPs was measured as 28.55 Å and 16.56 Å, respectively, utilizing the Deby–Scherrer equation:

$$D = \frac{k\lambda}{\beta\cos\theta} \tag{5}$$

where k is a constant, 0.9, λ the wavelength, β (the fullwidth at half-maximum, and θ the Bragg diffraction angle.

The variation in the results can be described by the disparity in ionic radii of Nd^{3+} (1.12 Å), Fe^{2+} (0.83 Å), and Al^{3+} (0.57 Å). It was noted that the average crystallite size decreased and that there was a slight shift in peaks, indicating the successful formation of Nd-doped $FeAl_2O_4$ NPs.[37] Figure 2b displays Raman spectra of the $FeAl_2O_4$ and Nd-doped $FeAl_2O_4$ NPs acquired at room temperature. In the $FeAl_2O_4$ material, distinct peaks at approximately 91.44 cm^{-1}, 217.53 cm^{-1}, 346.66 cm^{-1}, 564.64 cm^{-1}, 669.18 cm^{-1}, and 736.13 cm^{-1} can be observed, indicating the presence of acoustic combinations. The peak at 91.44 cm^{-1} corresponds to the transverse acoustic mode (2TA). Further, a peak emerges at 217.53 cm^{-1} with A1 symmetry, complementing the existing 2TA mode, and a peak is observed at 346.66 cm^{-1} (E1 symmetry), indicating the existence of the E_1 (TO) mode. Further peaks at 564.64 cm^{-1}, 669.18 cm^{-1}, and 736.13 cm^{-1} correspond to specific symmetries and modes. These include A1 symmetry with M − K points for the first peak and combinations of transverse acoustic and transverse optical (TA + TO) with H and M points and longitudinal acoustic and transverse optical (LA + TO) with an M point for the second and third peaks, respectively.[38] In addition, including the Nd dopant caused a slight decrease in the wavenumbers of the vibrational modes of $FeAl_2O_4$. It is worth noting that there was an observed increase in peak intensity in the Nd-doped $FeAl_2O_4$ NPs, which suggests that Nd ions have been successfully incorporated into the $FeAl_2O_4$ structures.

Figure 3a, b exhibits SEM images of $FeAl_2O_4$ and Nd-doped $FeAl_2O_4$ NPs. The $FeAl_2O_4$ images (Fig. 3a) reveal NPs with an irregular shape and a certain degree of aggregation. In addition, the Nd-doped $FeAl_2O_4$ sample (Fig. 3b) demonstrates enhanced NP morphology with reduced aggregation, leading to improved electrochemical activities. In addition, the elemental composition was evaluated by EDX investigation in Fig. 3c, d. This analysis of $FeAl_2O_4$ (Fig. 3c) revealed the existence of Fe, Al, C, and O elements with no impurity peaks, indicating the high purity of the material. Further, the Nd-doped $FeAl_2O_4$ NPs displayed in Fig. 3d show the presence of Nd, Fe, Al, C, and O elements in appropriate amounts. This observation validates the inclusion of Nd within the $FeAl_2O_4$ lattice structures.

To analyze the surface area (SA) of the $FeAl_2O_4$ and Nd-doped $FeAl_2O_4$ NP material, the BET measurement technique was employed. Figure 4 illustrates isotherms of $FeAl_2O_4$ and Nd-doped $FeAl_2O_4$ NPs which shows a type III isotherm with a mesoporous structure.[31] By analyzing the N_2 adsorption/desorption isotherm, it was discovered that the SAs of $FeAl_2O_4$ and Nd-doped $FeAl_2O_4$ NPs were 79.47 $m^2\ g^{-1}$ and 111.15 $m^2\ g^{-1}$, respectively. The unique structure of Nd-doped $FeAl_2O_4$ NPs with a large SA allows for enhanced accessibility of electrolyte ions and facilitates efficient intercalation and de-intercalation processes, resulting in enhanced electrochemical capacities of Nd-doped $FeAl_2O_4$ NPs.

Electrochemical Measurements

The electrochemical properties of the $FeAl_2O_4$ and Nd-doped $FeAl_2O_4$ NPs electrodes analysis were involved, using CV in a conventional three-electrode system. The CV curves for the $FeAl_2O_4$ and Nd-doped $FeAl_2O_4$ NPs electrode materials with a potential of 0.0–0.75 V at scan rates of 5 mV s^{-1}, 10 mV s^{-1}, 20 mV s^{-1}, and 30 mV s^{-1} are shown in Fig. 5a, b. From the CV curves, it can be observed that the current steadily increases as the scan rate rises. This suggests a direct relationship between voltametric current and scan rate. In addition, distinctive peaks of the cyclic voltammograms of the $FeAl_2O_4$ and Nd-doped $FeAl_2O_4$ NPs electrodes were the result of the redox reaction contributing to the pseudocapacitive nature suggesting a straightforward and reversible oxidation and reduction process.[33] Surprisingly, the Nd-doped $FeAl_2O_4$ NPs electrode material exhibited robust redox peaks with a larger loop area, potentially indicating a stronger synergistic consequence between the Nd, Fe, and Al ions. These features have the potential to expand the performance of spinel-structured electrodes in electrochemical analysis.

The Cs of the $FeAl_2O_4$ and Nd-doped $FeAl_2O_4$ NPs electrodes was determined utilizing Eq. 1, which exhibited 588.78 F g^{-1} and 908.59 F g^{-1},

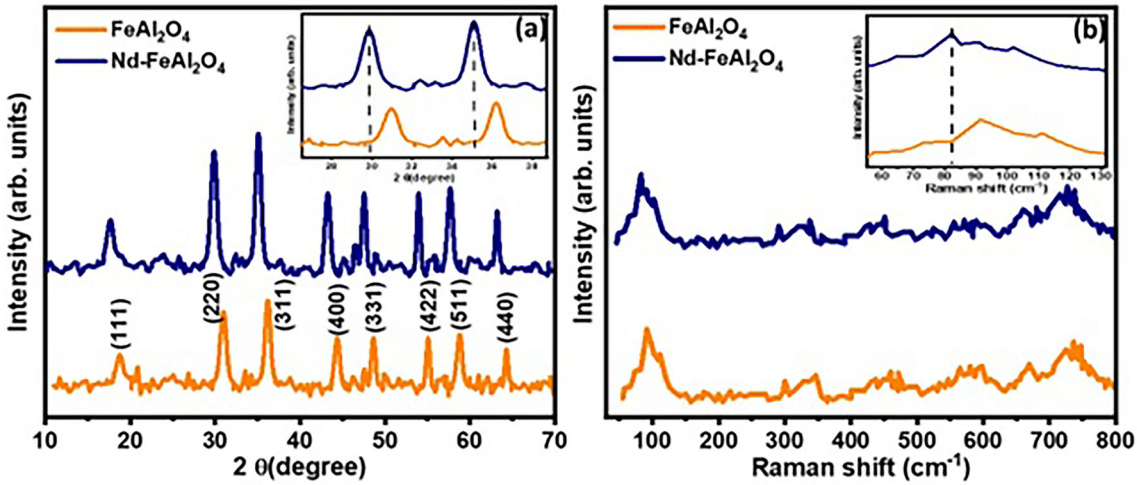

Fig. 2. (a) XRD pattern of $FeAl_2O_4$ and Nd-doped $FeAl_2O_4$ NP_s, (b) Raman ranges of $FeAl_2O_4$ and Nd-doped $FeAl_2O_4$ NPs.

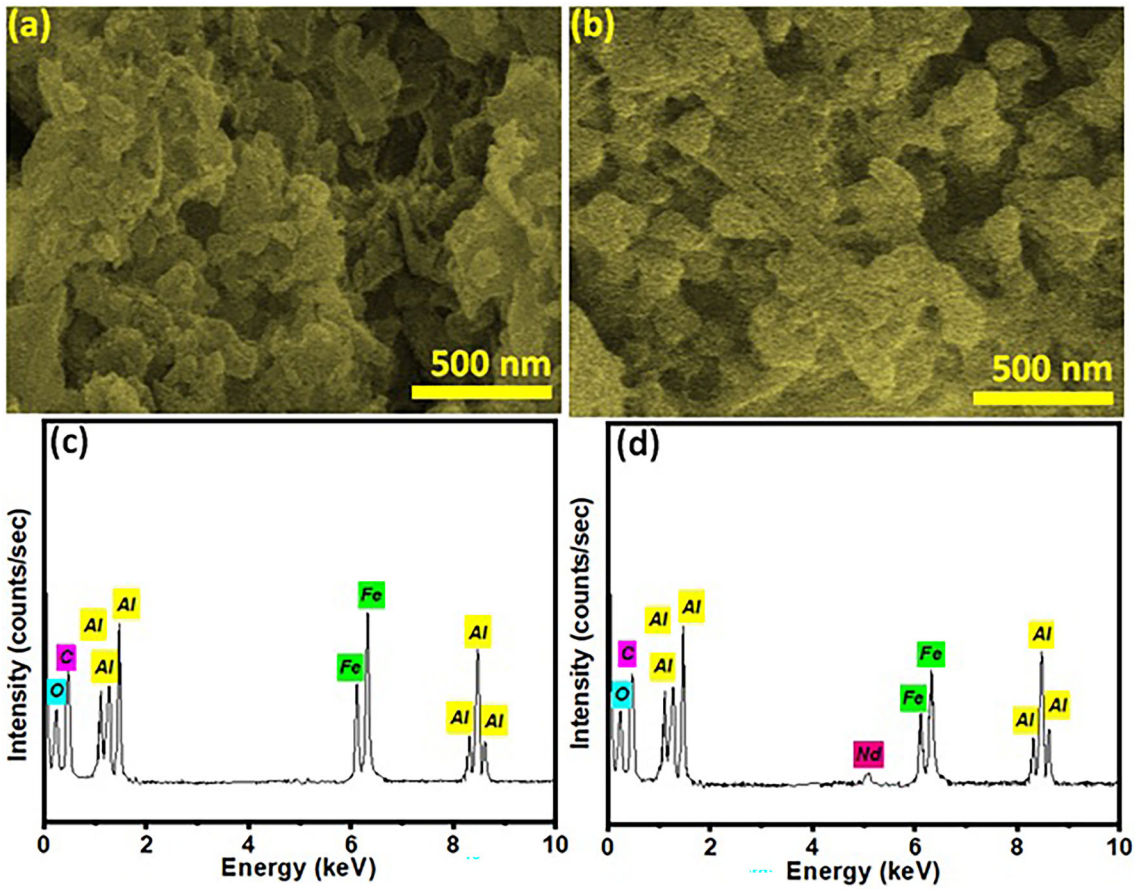

Fig. 3. Scanned images of (a) $FeAl_2O_4$, (b) Nd-doped $FeAl_2O_4$ NP_s and EDX spectra of, (c) $FeAl_2O_4$, (d) Nd-doped $FeAl_2O_4$ NPs.

respectively, at 5 mV s^{-1}. The enhanced Cs of the Nd-doped $FeAl_2O_4$ NPs electrode can be explained by the strong redox peaks observed, suggesting a larger active area and extra electroactive sites, which allow for better contact and accessibility to aqueous electrolyte ions during the analysis. When the scan rate was increased, the redox peaks moved towards extreme (high and low) potentials (Fig. 5c), suggesting that there was a higher diffusion resistance for ions inside the electrode.[39] In addition, a graph between the Cs of the $FeAl_2O_4$ and Nd-doped $FeAl_2O_4$ NPs electrodes versus scan rate i shown in

Fig. 5d. The Cs value declined as the scan rate increased. Interestingly, when the scan rate was increased, diffusion of the electrolyte ions was hindered by internal resistance and polarization. In contrast, as the scan rate was reduced, active sites on both the inner and outer interfaces of the material contributed to providing a comparatively developed Cs.[40]

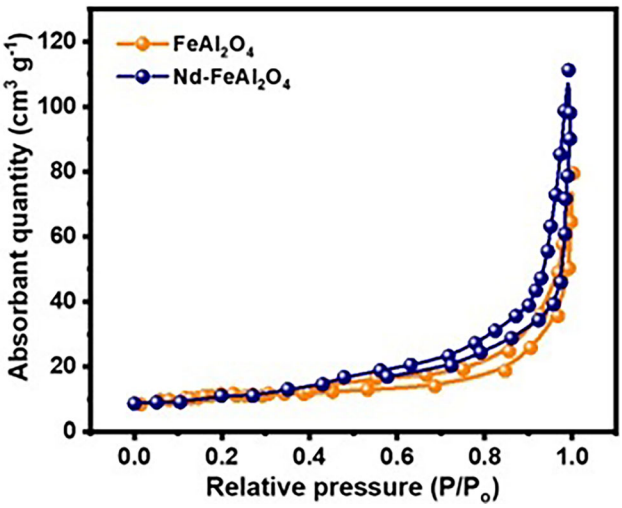

Fig. 4. BET isotherms of Nd-doped $FeAl_2O_4$ NPs.

To gain a deeper insight into the behavior of the $FeAl_2O_4$ and Nd-doped $FeAl_2O_4$ NPs electrodes for supercapacitor (SC) applications, we conducted GCD measurements. Fig. 6a, b displays GCD curves at 1–3 A g^{-1} compared to Ag/AgCl for the $FeAl_2O_4$ and Nd-doped $FeAl_2O_4$ NPs electrodes. It is worth mentioning that the Nd-doped $FeAl_2O_4$ NPs electrode has a longer discharge time compared to $FeAl_2O_4$ electrodes. These findings indicate that the enhanced capacitive behavior was due to the electrode's greater surface area and the presence of a mesoporous structure. Additionally, the Cs of the $FeAl_2O_4$ and Nd-doped $FeAl_2O_4$ NPs electrodes was analyzed using Eq. 2. It is worth noting that the Nd-doped $FeAl_2O_4$ NPs electrode reveals a Cs of 1194.69 F g^{-1}, significantly surpassing that of $FeAl_2O_4$ (697.73 F g^{-1}) at 1 A g^{-1}. The GCD profile showed that, as the current density rises, the discharge time decreases with a decreasing trend of Cs (Fig. 6c). This suggests that, at 3 A g^{-1} current density, entirely active sites were not available for electrolyte ions to carry out electrochemical reactions.[41] The specific power (P_d) and specific energy

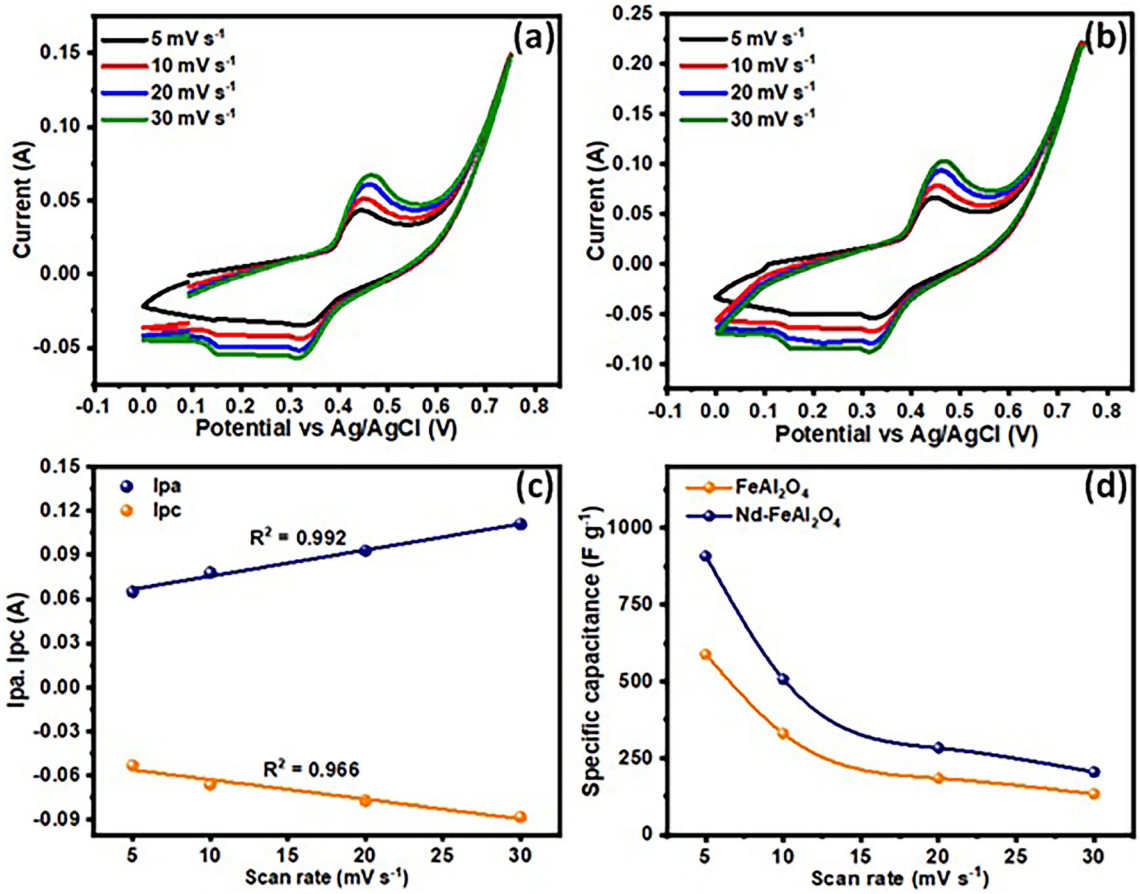

Fig. 5. Voltammograms of (a) $FeAl_2O_4$, (b) Nd-doped $FeAl_2O_4$ NP_s, (c) anodic/cathodic peak shifting, (d) specific capacitance vs scan rate.

Table I. Comparison of Nd-doped $FeAl_2O_4$ NPs between literature reports

No	Material	Specific capacitance (F g^{-1})	Current density (A $g^{-1)}$	Electrolyte (*MKOH*)	References
1	Mo-$ZnAl_2O_4$	1477.63	1.0	2.0	31
2	Ce-$CoFe_2O_4$	937.50	0.5	1.0	42
3	Mn-$ZnCo_2O_4$	707.45	0.5	1.0	43
4	Dy-$ZnSm_2O_4$	1908.5	0.03	2.0	9
5	Ag-$MnCo_2O_4$	942.54	1.0	6.0	44
6	Cr-$MgAl_2O_4$	955.34	1.0	2.0	45
7	Zn-$MnCo_2O_4$	720.54	0.5	2.0	46
8	Nd-$FeAl_2O_4$	1194.69	1.0	2.0	This work

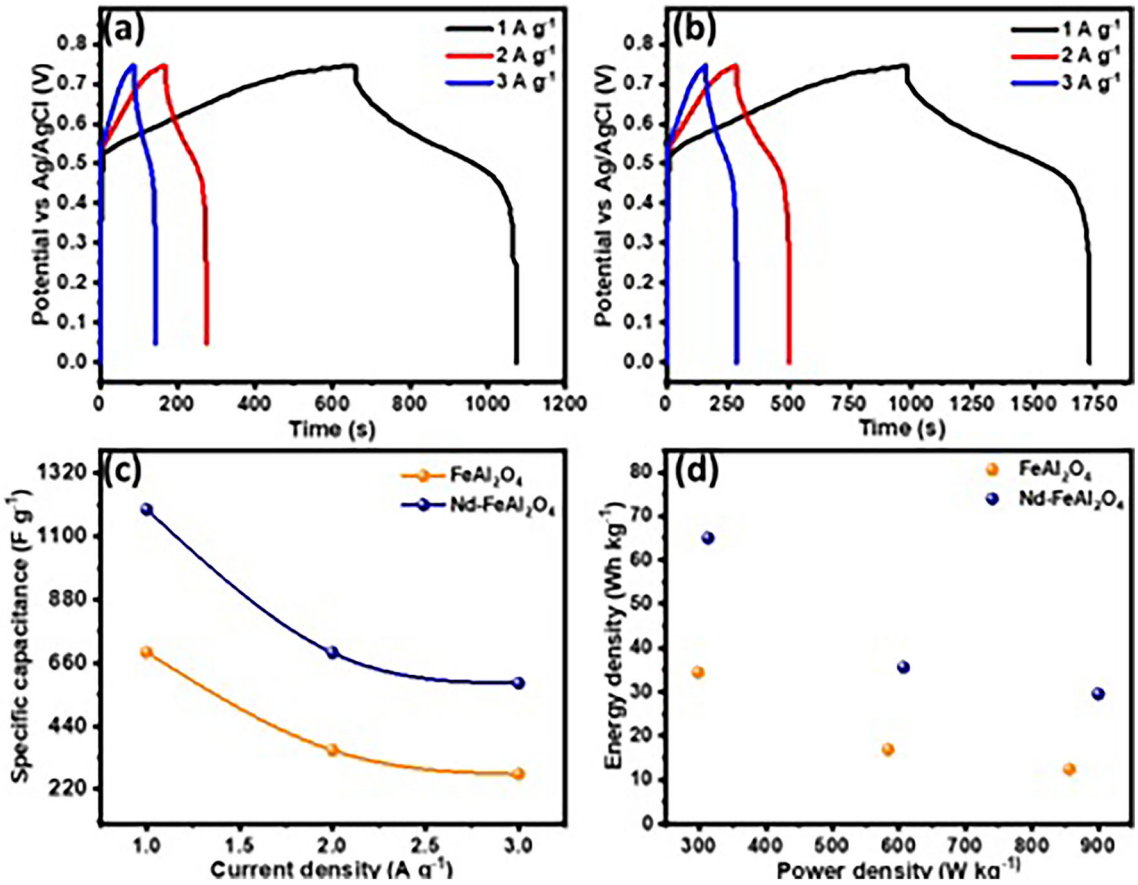

Fig. 6. GCD profile of (a) $FeAl_2O_4$, (b) Nd-doped $FeAl_2O_4$ NP_s, (c) specific capacitance vs current density of $FeAl_2O_4$ and Nd-doped $FeAl_2O_4$ NP_s, (d) graph between E_d and P_d of $FeAl_2O_4$ and Nd-doped $FeAl_2O_4$ NPs.

(E_d) were derived from the GCD curve by Eqs. 3 and 4, as shown in Fig. 6d. However, Nd-doped $FeAl_2O_4$ NPs exhibit a maximum specific power of 313 W kg^{-1} and specific energy of 65 Wh kg^{-1} at 1 A g^{-1}. The Cs at different current densities with the electrolytes achieved in this study and reported for previous doped spinel-based electrodes are displayed in Table I.

The synthesized material underwent analysis using EIS and Nyquist plots (Fig. 7a) of the $FeAl_2O_4$ and Nd-doped $FeAl_2O_4$ NPs electrodes clearly demonstrating a comprehensive examination of the internal resistive characteristics between the electrolyte and the electrode. At higher frequencies, the intercept reveals the presence of electrolyte resistance (Rs) that emerges from the interaction of ionic and electrical components. The size of the semi-circle reflects the level of resistance that occurs when a charge is transferred (R_{ct}) between the electrode and the electrolyte. R_{ct} includes the resistance that occurs within particles themselves, as well as the resistance that occurs between the

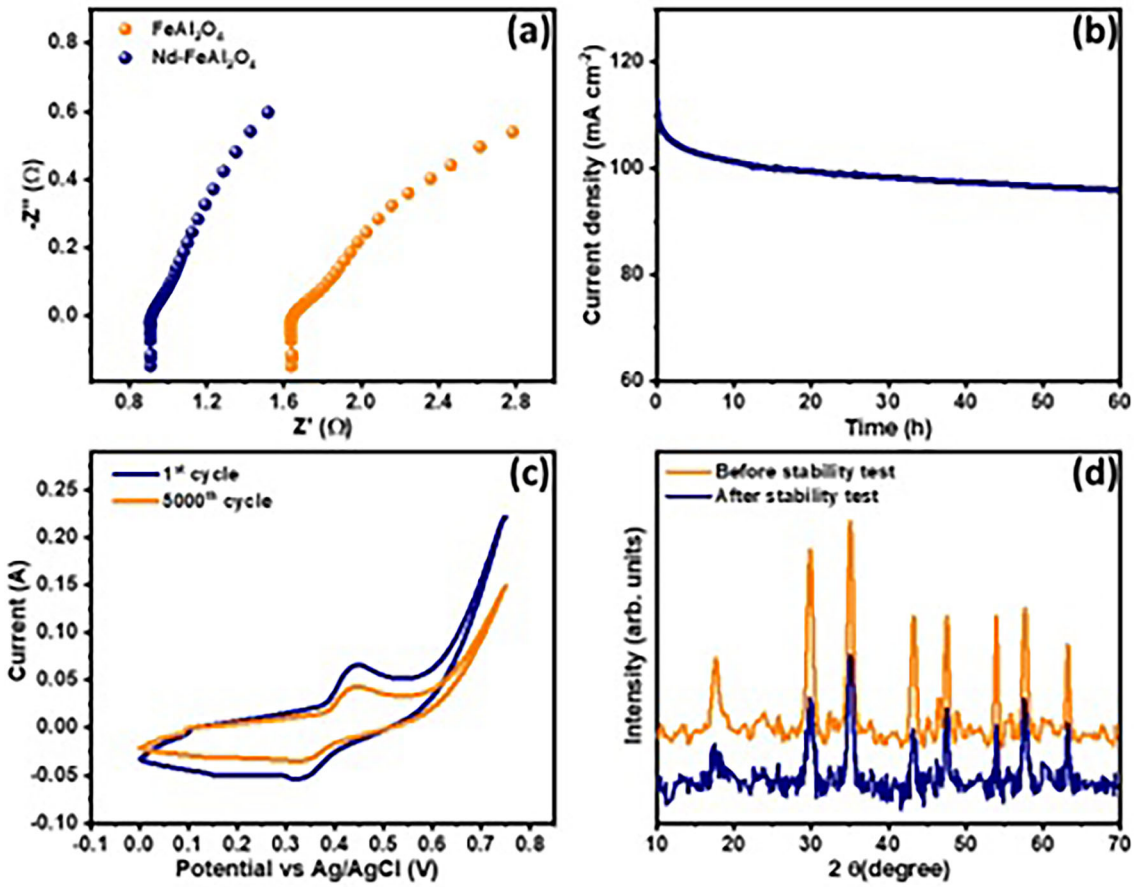

Fig. 7. (a) Nyquist plot of Nd-doped $FeAl_2O_4$ NP_s, (b) stability test of Nd-doped $FeAl_2O_4$ NP_s, (c) CV stability test of Nd-doped $FeAl_2O_4$ NP_s, (d) XRD stability test of Nd-doped $FeAl_2O_4$ NPs.

particles and the current collector. The R_s value for the $FeAl_2O_4$ (1.63 Ω) and Nd-doped $FeAl_2O_4$ NPs electrodes was found to be 0.9 Ω. The Nd-doped $FeAl_2O_4$ NPs electrode exhibited a low R_{ct} value of 0.07 Ω, while the $FeAl_2O_4$ electrode had 0.12 Ω. These results suggest that the Nd-doped $FeAl_2O_4$ NPs electrode exhibited very low levels of charge transfer and electrolyte resistance. This feature enhanced the conductivity between the electrode and electrolyte, making it easier to insert and remove ions from the electrode surface.[47] The chronoamperometric method was employed to assess the stability and electrochemical performance of the Nd-doped $FeAl_2O_4$ NPs electrode. From Fig. 7b, it is obvious that the current density of the Nd-doped $FeAl_2O_4$ NPs electrode initially decreased, with the drop rate being significant in the earlier period, but, later on, it exhibited a stable behavior for 60 h. This indicates that the Nd-doped $FeAl_2O_4$ NP*s* electrode had a highly responsive electrochemical behavior and stable electrochemical properties. In order to ascertain the longevity of the supercapacitor, it was crucial to examine its cyclic stability and reversibility. The cyclic stability of the electrode made of Nd-doped $FeAl_2O_4$ NPs was evaluated (Fig. 7c) by subjecting it to 5000 cycles at 5 mVs^{-1}.The image clearly demonstrates that, even after the 5000th CV cycle, no significant changes were observed. The results demonstrate exceptional durability throughout extended cycling. Additionally, it was clear from the XRD pattern (Fig. 7d) that the phase and structure of the Nd-doped $FeAl_2O_4$ NPs electrode material remained intact, which suggests that there was an increased level of electrolyte ion transport within the active electrode material.[8]

CONCLUSION

An efficient technique involving sonication was employed to successfully synthesize Nd-doped $FeAl_2O_4$ nanoparticles (NPs), which can be employed in energy storage applications. The electrochemical measurements of the NPs was investigated and found to exhibit a substantial enhancement in the specific capacitance (Cs) of 1194.69 F g^{-1} at 1 A g^{-1} and greater specific energy (65 Wh kg^{-1}) and specific power (313 W kg^{-1}). The Nd-doped $FeAl_2O_4$ NPs electrode showed a remarkable reduction in impedance characteristics (R_s = 0.9 Ω, R_{ct} = 0.07 Ω) while maintaining an exceptional cycle stability of 60 h after 5000 cycles.

Therefore, the Nd-doped $FeAl_2O_4$ NPs electrode exhibits immense potential as material for supercapacitor (SC) applications due to its cost-effective precursor, energy-efficient synthesis process, and outstanding electrochemical performance.

ACKNOWLEDGEMENTS

The Deanship of Scientific Research at King Khalid University is greatly appreciated for funding (R.G.P-1/356/44). The authors express their gratitude to Princess Nourah bint Abdulrahman University Researchers Supporting Project number (PNURSP2024R132), Princess Nourah bint Abdulrahman University, Riyadh, Saudi Arabia. A.M.A. Henaish thanks the the Ministry of Science and Higher Education of the Russian Federation (Ural Federal University Program of Development within the Priority-2030 Program) is gratefully acknowledged.

AUTHOR CONTRIBUTIONS

Every author has made an equal contribution.

DATA AVAILABILITY STATEMENTS

The author will make the datasets generated and/or analyzed during the current work available upon reasonable request.

COMPETING INTERESTS

This work has no conflicts of interest of any kind.

ETHICAL APPROVAL

The ethical rules of the journal are adhered to by this paper.

REFERENCES

1. M. Hussain, S.D. Alahmari, F.F. Alharbi, S.R. Ejaz, M. Abdullah, S. Aman, A.G. Al-Sehemi, A.M.A. Henaish, A. Sadaf, and H.M.T. Farid, *J. Energy Storage* 80, 110289 (2024).
2. S. Khan, M. Usman, M. Abdullah, M. Suleman Waheed, M. Faheem Ashiq, M. Ishfaq Ahmad, A.M. Karami, M. Fahad Ehsan, S. Manzoor, and M. Naeem Ashiq, *Fuel* 357, 129688 (2024).
3. A.M. Alenad, N. Ahmad, S. Aman, M. Noman Saeed, H.M.T. Farid, and T.A.M. Taha, *J. Taibah Univ. Sci.* 17, 2231132 (2023).
4. F. Qi, X. Lu, Y. Wang, H. Zhang, A. Trukhanov, and Z. Sun, *J. Colloid Interface Sci.* 607, 1253 (2022).
5. M. Hayat, M. Abdullah, K. Jabbour, N. Bibi, S. Khan, B. Ali, A.M. Karami, M.F. Ehsan, and M.N. Ashiq, *Mater. Chem. Phys.* 310, 128436 (2023).
6. F. Qi, L. Shao, X. Shi, F. Wu, H. Huang, Z. Sun, and A. Trukhanov, *J. Colloid Interface Sci.* 601, 669 (2021).
7. M. Hussain, M.M. Alanazi, S.A.M. Abdelmohsen, S.D. Alahmari, M. Abdullah, S. Aman, A. Dahshan, A.M.A. Henaish, Z. Ahmad, and H.M.T. Farid, *J. Energy Storage* 84, 110920 (2024).
8. M. Ali, S.D. Alahmari, S.A.M. Abdelmohsen, M.M. Alanazi, A.G. Al-Sehemi, M. Abdullah, S. Aman, and H.M.T. Farid, *Ceram. Int.* 50, 6931 (2024).
9. S. Ahmad, K. Jabbour, M. Rafeeq, A. Naz, K.F. Fawy, S. Manzoor, M. Abdullah, N. Ghazouani, A. Mir, and M.N. Ashiq, *Ceram. Int.* 49, 28036 (2023).
10. S. Aman, S. Gouadria, F. F. Alharbi, M. N. Saeed, and H. M. T. Farid, *JOM* 1 (2023).
11. S. Wang, L. Shao, L. Yu, J. Guan, X. Shi, Z. Sun, J. Cai, H. Huang, and A. Trukhanov, *Energy Technol.* 9, 2100298 (2021).
12. X. Zhang, Y. Tang, F. Zhang, and C.-S. Lee, *Adv. Energy Mater.* 6, 1502588 (2016).
13. M. Wang, C. Jiang, S. Zhang, X. Song, Y. Tang, and H.M. Cheng, *Nat. Chem.* 10, 667 (2018).
14. Y. Zhang, H. Gao, J. Wang, Q. Chi, T. Zhang, C. Zhang, Y. Feng, Y. Zhang, D. Cao, and K. Zhu, *Inorg. Chem. Front.* 11, 1289 (2024).
15. X. Zhao, B. Fan, N. Qiao, R.A. Soomro, R. Zhang, and B. Xu, *Appl. Surf. Sci.* 642, 158639 (2024).
16. S. Guan, J. Zhou, S. Sun, Q. Peng, X. Guo, B. Liu, X. Zhou, and Y. Tang, *Adv. Funct. Mater.* 2314890 (2024).
17. R. Yang, W. Yao, L. Zhou, F. Zhang, Y. Zheng, C. S. Lee, and Y. Tang, *Adv. Mater.* 2314247 (2024).
18. M. Abdullah, F.F. Alharbi, R.Y. Khosa, H.A. Alburaih, S. Manzoor, A.G. Abid, H.E. Ali, M.S. Waheed, M.N. Ansari, and H.M.T. Farid, *Korean J. Chem. Eng.* 40, 1518 (2023).
19. N.A. Althubiti, M.M. Hassan, M.S. Waheed, S. Aman, R.Y. Khosa, H.M.T. Farid, A. Nazir, M.Z. Ansari, F. Abdulaziz, and T.A.M. Taha, *J. Energy Storage* 70, 108154 (2023).
20. S. Manzoor, S.V. Trukhanov, M.N. Ansari, M. Abdullah, A. Alruwaili, A.V. Trukhanov, M.U. Khandaker, A.M. Idris, K.S. El-Nasser, and T.A. Taha, *Nanomater.* 12, 2209 (2022).
21. M. Hussain, B.M. Alotaibi, A.W. Alrowaily, H.A. Alyousef, M.F. Alotiby, M. Abdullah, A.G. Al-Sehemi, A.M.A. Henaish, Z. Ahmad, and S. Aman, *J. Phys. Chem. Solids* 188, 111919 (2024).
22. S. Mu, Q. Liu, P. Kidkhunthod, X. Zhou, W. Wang, and Y. Tang, Natl. Sci. Rev. 8 (2021).
23. Z. Huang, P. Luo, S. Jia, H. Zheng, and Z. Lyu, *J. Phys. Chem. Solids* 167, 110746 (2022).
24. M. Hussain, M.M. Alanazi, S.A.M. Abdelmohsen, S.D. Alahmari, M. Abdullah, S. Aman, A.G. Al-Sehemi, A.M.A. Henaish, Z. Ahmad, and H.M.T. Farid, *Diam. Relat. Mater.* 142, 110764 (2024).
25. D.A. Alshammari, Y.M. Riyad, S. Aman, N. Ahmad, H.M. Tahir Farid, and Z.M. El-Bahy, *J. Electroanal. Chem.* 945, 117701 (2023).
26. A.G. Abid, S. Gouadria, S. Manzoor, K.M.S. Katubi, K. Jabbour, M. Abdullah, M. Un Nisa, S. Aman, M.S. Al-Buriahi, and M.N. Ashiq, *Fuel* 336, 127066 (2023).
27. S.A. Habib, S.A. Saafan, T.M. Meaz, M.A. Darwish, D. Zhou, M.U. Khandaker, M.A. Islam, H. Mohafez, A.V. Trukhanov, S.V. Trukhanov, and M.K. Omar, *Nanomater.* 12, 931 (2022).
28. T. Zahra, M.M. Alanazi, S.D. Alahmari, S.A.M. Abdelmohsen, M. Abdullah, S. Aman, A.G. Al-Sehemi, A.M.A. Henaish, Z. Ahmad, and H.M. Tahir Farid, *Int. J. Hydrogen Energy* 59, 97 (2024).
29. H. Donya, S. Aman, N. Ahmad, H. M. Tahir Farid, and T. A. Mohaymen Taha, Int. J. Hydrogen Energy (2023).
30. M. Abdullah, M.Z. Ansari, Z. Ahamd, P. John, S. Manzoor, A.M. Shawky, H.H. Hegazy, A.H. Chughtai, M.N. Ashiq, and T.A. Taha, *Ceram. Int.* 49, 6780 (2023).
31. N.A. Althubiti, S. Aman, and T.A.M. Taha, *Ceram. Int.* 49, 27496 (2023).
32. T. Tao, J. He, Y. Wang, X. Shi, L. Shao, A. Trukhanov, and Z. Sun, *J. Power. Sources* 539, 231457 (2022).
33. X. Li, S. Aftab, S. Hussain, F. Kabir, A.M.A. Henaish, A.G. Al-Sehemi, M.R. Pallavolu, and G. Koyyada, *J. Mater. Chem. A* 12, 4421 (2024).
34. Z. Huang, P. Luo, Q. Wu, and H. Zheng, *J. Phys. Chem. Solids* 161, 110479 (2022).
35. X. Li, S. Aftab, A. Abbas, S. Hussain, M. Aslam, F. Kabir, H.S.M. Abd-Rabboh, H.H. Hegazy, F. Xu, and M.Z. Ansari, *Nano Energy* 118, 108979 (2023).

36. T. Wei, Y. Zhou, C. Sun, X. Guo, S. Xu, D. Chen, and Y. Tang, Nano Res. **1** (2023).
37. M. K. Tufail, P. Zhai, M. Jia, N. Zhao, and X. Guo, Energy Mater. Adv. **4** (2023).
38. S. Aman, N. Ahmad, M.B. Tahir, M.M. Alanazi, S.A.M. Abdelmohsen, R.Y. Khosa, and H.M.T. Farid, *Surf. Interfaces* 38, 102857 (2023).
39. G. Liu, Y. Yang, X. Lu, F. Qi, Y. Liang, A. Trukhanov, Y. Wu, Z. Sun, X. Lu, and A.C.S. Appl, *Mater. Interfaces* 14, 31803 (2022).
40. R.S. Gohar, S. Manzoor, T. Munawar, S. Gouadria, M.F. Ashiq, F. Iqbal, F. Aftab, M. Najam-Ul-Haq, A.V. Trukhanov, and M.N. Ashiq, *J. Energy Storage* 52, 104930 (2022).
41. V.S. Kumbhar, A.D. Jagadale, N.M. Shinde, and C.D. Lokhande, *Appl. Surf. Sci.* 259, 39 (2012).
42. C. Wang, P. Shi, C. Guo, R. Guo, and J. Qiu, *J. Electroanal. Chem.* 956, 118072 (2024).
43. B. Liu, X. Wang, Y. Chen, H. Xie, X. Zhao, A.B. Nassr, and Y. Li, *J. Energy Storage* 68, 107826 (2023).
44. Z. Huang, Y. Zhang, H. Wang, and J. Li, Appl. Phys. Lett. **123** (2023).
45. M. Abdullah, N. Alwadai, M. Al Huwayz, S. Manzoor, P. John, A.G. Abid, M.I. Ghouri, S. Aman, M.S. Al-Buriahi, and M.N. Ashiq, *Energy Fuels* 37, 1297 (2023).
46. D. Alhashmialameer, S. Aman, M. Abdullah, R. Y. Khosa, S. Manzor, H. M. Ali, M. H. Helal, H. M. T. Farid, M. S. Waheed, and T. A. Taha, J. Sol-Gel Sci. Technol. 1 (2022).
47. Z. Liang, F. Du, N. Zhao, and X. Guo, *Chin. J. Struct. Chem.* 42, 100108 (2023).